The Nonlinear One-Way Navier-Stokes (NOWNS) Approach for Boundary-Layer Transition

Michael K. Sleeman* and Tim Colonius†
California Institute of Technology, Pasadena, CA, USA

Matthew T. Lakebrink‡
Boeing Research & Technology, Hazelwood, MO, 63042, United States

This work seeks rapid prediction of laminar-to-turbulent transition based on first principles, rather than commonly employed empirical correlations. The nonlinear one-way Navier-Stokes (NOWNS) equations were recently applied to the early stages of boundary layer transition where it was demonstrated that NOWNS can accurately replicate direct numerical simulation (DNS) results with similar accuracy to the nonlinear parabolized stability equations (NPSE). While having greater computational cost than NPSE, NOWNS is a more robust, convergent parabolization of the governing equations and is expected to succeed for stronger nonlinearity where NPSE fails. We demonstrate that NOWNS succeeds for stronger nonlinearity by applying it to an oblique-wave breakdown case where NPSE fails. In addition, we demonstrate that NOWNS supports non-modal disturbances in the form of random noise applied to the inlet boundary condition of the oblique-wave breakdown case, and a blowing/suction strip for a K-type (fundamental) transition case.

I. Introduction

Hydrodynamic stability analysis is a critical tool for predicting laminar-turbulent transition in boundary layer flows. Modern industry tools use linear theory to predict transition onset, often using either the e^N-method [1, 2] or the variable N-factor approach [3] to extrapolate through nonlinear transition. Fundamentally, transition can be studied using direct numerical simulation (DNS) [4–6], but this approach is limited by its large computational cost. The nonlinear parabolized stability equations (NPSE) entail a much lower computational cost [7], but convergence issues limit its use to the early stages of transition [8, 9]. Even in the linear case, however, PSE is unable to (accurately) track non-modal and multi-modal instabilities [9], and its minimum step size for stability prevents capturing all length scales in the streamwise direction, which is particularly problematic when extending to the nonlinear regime.

Linear OWNS overcomes these limitations of linear PSE, but at a greater computational cost. The OWNS approach does not have a minimum step size for stability, which means that arbitrarily small steps can be taken to resolve all of the length scales, enabling OWNS to capture non-modal and multi-modal interactions. The linear OWNS approach has previously been applied to two-dimensional (2D) and three-dimensional (3D) boundary-layer flows [10]. In particular, linear OWNS approach has proven useful for hypersonic boundary layer flows [11–13] where classical stability analysis methods often fail. Previous work on linear OWNS has demonstrated its robustness, which makes it well-suited to nonlinear stability analysis. More recently, the linear OWNS procedure has been extended to support nonlinear effects in the nonlinear OWNS (NOWNS) framework [14].

In this paper, we demonstrate the advantages of NOWNS with respect to nonlinear PSE (NPSE). In section II we present the governing equations and summarize the details of the method. In section III, we demonstrate the nonlinear OWNS approach for 3D boundary-layer flows. Finally, in section IV we present plans for future work.

II. Method

The NOWNS approach was previously presented in [14] and we summarize it briefly here. The compressible Navier-Stokes equations are written in Cartesian coordinates in terms of the specific volume ν, velocity $\boldsymbol{u} = (u, v, w)$,

*PhD Candidate, Mechanical and Civil Engineering.
†Frank and Ora Lee Marble Professor of Mechanical Engineering and Medical Engineering.
‡Boeing Associate Technical Fellow.

and pressure p:

$$\frac{D\nu}{Dt} - \nu(\nabla \cdot \boldsymbol{u}) = 0, \tag{1a}$$

$$\frac{D\boldsymbol{u}}{Dt} + \nu\nabla p = \frac{1}{Re}\nu\nabla^2\boldsymbol{u}, \tag{1b}$$

$$\frac{Dp}{Dt} + \gamma p(\nabla \cdot \boldsymbol{u}) = \frac{\gamma}{PrRe}(\nu\nabla^2 p + p\nabla^2\nu). \tag{1c}$$

We have nondimensionalized the equations using the free-stream speed of sound (c_∞), the free-stream specific volume (ν_∞), the Blasius length scale ($\delta_0 = \sqrt{\frac{x_0\nu_\infty\mu_\infty}{c_\infty}}$), and the free-stream fluid properties. This study focuses on low-speed boundary layer flows, so we approximate the fluid as a perfect gas with constant fluid properties.

We define a vector of flow quantities $\boldsymbol{q} = (\nu, u, v, w, p)$ and write the equations in operator form as

$$\frac{\partial \boldsymbol{q}}{\partial t} + A(\boldsymbol{q})\frac{\partial \boldsymbol{q}}{\partial x} + B_y(\boldsymbol{q})\frac{\partial \boldsymbol{q}}{\partial y} + B_z(\boldsymbol{q})\frac{\partial \boldsymbol{q}}{\partial z} + B_2(\boldsymbol{q})\Big(\frac{\partial^2 \boldsymbol{q}}{\partial x^2} + \frac{\partial^2 \boldsymbol{q}}{\partial y^2} + \frac{\partial^2 \boldsymbol{q}}{\partial z^2}\Big) \tag{2}$$

where the A and B operators are defined in appendix V.A. Here, x, y, z, correspond to the streamwise, transverse and spanwise directions, respectively.

A. Linear OWNS

We decompose the flow as

$$\boldsymbol{q}(x, y, z, t) = \bar{\boldsymbol{q}}(x, y, z) + \boldsymbol{q}'(x, y, z, t) \tag{3}$$

where $\bar{\boldsymbol{q}}$ is a time-invariant equilibrium solution (that we get by solving the Blasius equation), while $\boldsymbol{q}'$ is the disturbance variable for which we solve. We substitute the decomposition (3) into the equations (2) to obtain

$$A(\bar{\boldsymbol{q}})\frac{\partial \boldsymbol{q}'}{\partial x} = L(\bar{\boldsymbol{q}})\boldsymbol{q}' + \boldsymbol{f}. \tag{4}$$

where we have discarded terms that are nonlinear in $\boldsymbol{q}'$ and terms associated with $\partial^2\boldsymbol{q}'/\partial x^2$. Here, $\boldsymbol{f}$, is an exogeneous forcing function that represents these unmodeled physics (we neglect the streamwise diffusion terms because this simplifies the exposition, but it is possible to re-introduce these terms). We have also defined $C(\bar{\boldsymbol{q}})$ such that

$$C(\bar{\boldsymbol{q}})\boldsymbol{q}' = A(\boldsymbol{q}')\frac{\partial \bar{\boldsymbol{q}}}{\partial x} + B_y(\boldsymbol{q}')\frac{\partial \bar{\boldsymbol{q}}}{\partial y} + B_z(\boldsymbol{q}')\frac{\partial \bar{\boldsymbol{q}}}{\partial z} + B_2(\boldsymbol{q}')\Big(\frac{\partial^2 \bar{\boldsymbol{q}}}{\partial x^2} + \frac{\partial^2 \bar{\boldsymbol{q}}}{\partial y^2} + \frac{\partial^2 \bar{\boldsymbol{q}}}{\partial z^2}\Big), \tag{5}$$

and the linear operator $L(\bar{\boldsymbol{q}})$ such that

$$L(\bar{\boldsymbol{q}}) = -\frac{\partial}{\partial t} - B_y(\bar{\boldsymbol{q}})\frac{\partial}{\partial y} - B_z(\bar{\boldsymbol{q}})\frac{\partial}{\partial z} - B_2(\bar{\boldsymbol{q}})\Big(\frac{\partial^2}{\partial y^2} + \frac{\partial^2}{\partial z^2}\Big) - C(\bar{\boldsymbol{q}}). \tag{6}$$

To obtain a semi-discrete form of (4), we discretize in the wall-normal direction using a finite difference scheme (typically 4th-order central finite differences) which we represent using $D \approx \partial/\partial y$, while we assume that our disturbances are periodic in the spanwise direction with wavenumber β and in time with frequency ω so that our disturbance has the form

$$\boldsymbol{q}'(x, y, z, t) = \hat{\boldsymbol{q}}(x, y)e^{i(\beta z - \omega t)}. \tag{7}$$

Our semi-discrete linear operator becomes

$$L(\bar{\boldsymbol{q}}) = i\omega I - B_y(\bar{\boldsymbol{q}})D - i\beta B_z(\bar{\boldsymbol{q}}) - B_2(\bar{\boldsymbol{q}})(D^2 - \beta^2 I) - C(\bar{\boldsymbol{q}}), \tag{8}$$

This equation still supports upstream-going modes, which we can remove using a projection operator, as discussed in Towne et al. (2022) [15]. First we transform to characteristic variables, based on the eigen-decomposition of $A(\bar{\boldsymbol{q}})$, then we use the eigen-decomposition of the linear operator (in characteristic variables) to define a projection operator, $P(\bar{\boldsymbol{q}})$, that removes upstream-going modes. Using our projection operator, we obtain the parabolic (one-way) equation

$$\frac{\partial \boldsymbol{q}_+}{\partial x} = P(\bar{\boldsymbol{q}})A(\bar{\boldsymbol{q}})^{-1}[L(\bar{\boldsymbol{q}})\boldsymbol{q}_+ + \boldsymbol{f}], \tag{9}$$

where $\boldsymbol{q}_+ = P(\bar{\boldsymbol{q}})\boldsymbol{q}'$ is the downstream-going solution. In practice, we apply the projection operator using a recursive filtering approach to avoid taking the eigen-decomposition of the linear operator.

Since (9) is well-posed as a one-way equation, we can solve it numerically using a spatial-marching scheme. We discretize in the streamwise direction using a second-order backward differentiation formula (BDF2) scheme to obtain

$$\sum_{l=0}^{s-1} c^{(l)} \boldsymbol{q}_+^{(k+1-l)} = \Delta x P(\bar{\boldsymbol{q}}^{(k+1)}) A(\bar{\boldsymbol{q}}^{(k+1)})^{-1} [L(\bar{\boldsymbol{q}}^{(k+1)}) \boldsymbol{q}_+^{(k+1)} + \boldsymbol{f}^{k+1)}], \tag{10}$$

which can be solved numerically on a computer.

B. Nonlinear OWNS

We assumed previously that our disturbances are periodic in time and in the spanwise direction, so we can expand our disturbance variable into the Fourier series

$$\boldsymbol{q}'(x,y,z,t) = \sum_{m,n=-\infty}^{\infty} \hat{\boldsymbol{q}}_{mn} e^{i(n\beta z - m\omega t)}. \tag{11}$$

In linear OWNS, all Fourier modes evolve independently of each other, but they become coupled through the nonlinear terms so they cannot be considered separately in the nonlinear analysis. It is not possible to consider an infinite number of Fourier modes, so we truncate our Fourier series to obtain

$$\boldsymbol{q}'(x,y,z,t) = \sum_{m=-M}^{M} \sum_{n=-N}^{N} \hat{\boldsymbol{q}}_{mn} e^{i(n\beta z - m\omega t)}. \tag{12}$$

The previously discarded the nonlinear terms

$$\text{(NLT)} := A(\boldsymbol{q}')\frac{\partial \boldsymbol{q}'}{\partial x} + B_y(\boldsymbol{q}')\frac{\partial \boldsymbol{q}'}{\partial y} + B_z(\boldsymbol{q}')\frac{\partial \boldsymbol{q}'}{\partial z} + B_2(\boldsymbol{q}')\Big(\frac{\partial^2 \boldsymbol{q}'}{\partial x^2} + \frac{\partial^2 \boldsymbol{q}'}{\partial y^2} + \frac{\partial^2 \boldsymbol{q}'}{\partial z^2}\Big), \tag{13}$$

are reintroduced to obtain

$$A(\bar{\boldsymbol{q}})\frac{\partial \boldsymbol{q}'}{\partial x} = L(\bar{\boldsymbol{q}})\boldsymbol{q}' + \boldsymbol{F}(\boldsymbol{q}') + \boldsymbol{f}, \tag{14}$$

where we have defined

$$\boldsymbol{F}(\boldsymbol{q}') = -A(\boldsymbol{q}')\frac{\partial \boldsymbol{q}'}{\partial x} - B_y(\boldsymbol{q}')\frac{\partial \boldsymbol{q}'}{\partial y} - B_z(\boldsymbol{q}')\frac{\partial \boldsymbol{q}'}{\partial z} - B_2(\boldsymbol{q}')\Big(\frac{\partial^2 \boldsymbol{q}'}{\partial y^2} + \frac{\partial^2 \boldsymbol{q}'}{\partial z^2}\Big), \tag{15}$$

and we have included the streamwise diffusion terms in the forcing function.

We discretize the nonlinear terms so that they are consistent with the linear terms, and we compute Fourier components of the nonlinear terms using a Fast Fourier Transform (FFT), which we de-alias using the 3/2 rule. Our semi-discrete equations become

$$A(\bar{\boldsymbol{q}})\frac{\partial \hat{\boldsymbol{q}}_{mn}}{\partial x} = L_{mn}(\bar{\boldsymbol{q}})\hat{\boldsymbol{q}}_{mn} + \hat{\boldsymbol{F}}_{mn}(\boldsymbol{q}') + \hat{\boldsymbol{f}}_{mn}, \quad m = -M,\dots,M, \quad n = -N,\dots,N. \tag{16}$$

We use the projection operator from linear OWNS to obtain the one-way equation

$$\frac{\partial \hat{\boldsymbol{q}}_{+,mn}}{\partial x} = P_{mn}(\bar{\boldsymbol{q}})A(\bar{\boldsymbol{q}})^{-1}[L_{mn}(\bar{\boldsymbol{q}})\hat{\boldsymbol{q}}_{+,mn} + \hat{\boldsymbol{F}}_{mn}(\boldsymbol{q}_+) + \hat{\boldsymbol{f}}_{mn}], \quad m = -M,\dots,M, \quad n = -N,\dots,N. \tag{17}$$

Finally, we march this equation in space using the BDF2 scheme as

$$\sum_{l=0}^{s-1} c^{(l)} \hat{\boldsymbol{q}}_{+,mn}^{(k+1-l)} = P_{mn}(\bar{\boldsymbol{q}}^{(k+1)})A(\bar{\boldsymbol{q}}^{(k+1)})^{-1}[L_{mn}(\bar{\boldsymbol{q}}^{(k+1)})\hat{\boldsymbol{q}}_{+,mn}^{(k+1)} + \hat{\boldsymbol{F}}_{mn}(\boldsymbol{q}_+^{(k+1)}) + \hat{\boldsymbol{f}}_{mn}^{(k+1)}], \tag{18}$$

for $m = -M,\dots,M$ and $n = -N,\dots,N$. We note that for $\boldsymbol{q}'$ to be real-valued, we must have the condition $\hat{q}_{-mn} = \overline{\hat{q}_{mn}}$, so that we only need to solve the equations for $m = 0,\dots,M$ and $n = -N,\dots,N$.

1. Special treatment of the zero-frequency modes

In the previous work on nonlinear OWNS presented in Sleeman et al. (2023) [14], the equations for the zero-frequency modes were parabolized by neglecting the streamwise pressure gradient and the streamwise diffusion terms for these modes. More recently, we have successfully included the streamwise diffusion terms for the zero-frequency modes by using the recursion parameters presented in appendix V.C. However, we still found it necessary to neglect the streamwise pressure gradient for these modes. If we include the streamwise pressure gradient for the zero-frequency modes, we still achieve a numerically stable spatial march, but our results do not match those presented in the literature. We believe that the streamwise pressure gradient for the zero-frequency modes introduces upstream effects that corrupt the solution. The NOWNS procedure is able to remove the upstream effects of the streamwise pressure gradient to achieve a stable march, but in the process, the solution becomes inaccurate. NPSE for subsonic flows must also neglect the streamwise pressure gradient for the zero-frequency modes [16, 17], unless the pressure is removed in favor of the vorticity variables (for incompresible flows only) [7].

We have found that the effects of the streamwise diffusion terms for the zero-frequency modes is negligible. We have run all of the calculations presented in this paper both with and without these terms, and there is not a significant difference in the results. Therefore, it is generally not necessary to include these terms (and therefore generally not necessary to project the zero-frequency modes).

2. Spanwise symmetry

For the test cases we study here, the disturbance variable is constrained to be symmetric in the spanwise (z) direction, and the number of equations can be reduced. In primitive variables, all variables have even-symmetry, with the exception of the w-velocity which has odd-symmetry,

$$\begin{aligned}
\hat{\nu}_{m,-n} &= \hat{\nu}_{m,n}, \\
\hat{u}_{m,-n} &= \hat{u}_{m,n}, \\
\hat{v}_{m,-n} &= \hat{v}_{m,n}, \\
\hat{w}_{m,-n} &= -\hat{w}_{m,n}, \\
\hat{p}_{m,-n} &= \hat{p}_{m,n}.
\end{aligned}$$

The symmetry condition reduces the number of equations from $(M+1)\times(2N+1)$ to $(M+1)\times(N+1)$, so that we have roughly half the number of equations to solve.

3. Boundary conditions

At the wall, we impose no-slip isothermal boundary conditions ($u' = v' = w' = T' = 0$), while we solve for the specific volume, ν', at the wall using the (nonlinear) continuity equation. At the far-field boundary, we impose 1D (in y) inviscid Thompson characteristic boundary conditions to prevent spurious numerical reflections [18]. The inviscid assumption is valid because viscous effects from the boundary layer are negligible in the far-field. This choice of boundary conditions matches the boundary conditions used previously for linear OWNS [10, 11]. The Thompson characteristic boundary condition (as implemented in our code) is based on the linearized Navier-Stokes equations. However, this choice is reasonable because nonlinear effects are negligible far from the boundary layer.

Some previous work on PSE has used characteristic boundary conditions in the far-field [8]. However, other work has used the far-field boundary condition $\hat{\boldsymbol{q}}'_{mn}(y_{\max}) = 0$ [16]. The boundary layer must be allowed to grow in the wall-normal direction (due to nonlinear interactions), so we cannot have $\hat{v}'_{00}(y_{\max}) = 0$ for the mean-flow distortion (MFD). Instead, we must use either characteristic boundary conditions, or choose $\partial\hat{v}'_{00}/\partial y = 0$ at $y_{\max}$. The characteristic far-field boundary conditions are advantageous because they allow us to use the same boundary conditions for all modes, instead of handling the MFD as a separate case.

4. Streamwise diffusion terms

As noted above, neglecting the streamwise diffusion terms simplifies the parabolization procedure. Moreover, previous work on linear OWNS has reintroduced these terms (approximately) after parabolizing the equations, and found that their inclusion did not affect significantly the results of the stability calculation [11]. However, we have found that their impact on nonlinear OWNS is more pronounced, so we include them by discretizing second-streamwise derivatives using a second-order backward difference scheme, which is similar to the procedure used previously for

linear OWNS [11]. Provided the resulting equations are stable (which we verify *a posteriori*), then, apart from the parabolization error, the streamwise terms are included to $O(\Delta x^2)$.

5. Mean-flow distortion

The projection operators are linearized about the baseflow, and it could be argued that for nonlinear OWNS, the projection operators should be linearized about the full mean flow (including the effects of the mean flow distortion). It is straightforward to linearize about the corrected mean flow, as opposed to the base flow. We have tried doing so and found that it does not make a substantial difference in the results. It is more computationally efficient to linearize only about the base flow (for reasons we describe below), so we choose this approach moving forward.

6. Recursion parameters

The choice of recursion parameters is described in appendix V.C. These recursion parameters have previously been applied to subsonic linear OWNS and they have been demonstrated to match the results in the literature [10]. However, there is no guarantee that we can expect them to work well for nonlinear OWNS (particularly as we march farther downstream). We demonstrate *a posteriori* that this choice of recursion parameters works reasonably well, but it is possible that a better choice of recursion parameters exists.

III. Results

The NOWNS procedure was previously validated in Sleeman et al. (2023) [14], so we immediately present new results for oblique-wave breakdown. We choose a Mach number of Ma = 0.1 to study flows near the incompressible limit. In what follows, we normalize the streamwise coordinate as

$$\mathrm{Re}_x = \frac{U^*_\infty x^*}{\nu^*_\infty \mu^*_\infty},$$

while the wall-normal coordinate is normalized by

$$y = \frac{y^*}{\delta^*_0}.$$

We further specify the temporal frequency as

$$F = \frac{\omega^* \nu^*_\infty \mu^*_\infty}{U^{*2}_\infty},$$

and the spanwise wave number as

$$b = \frac{\beta^* \nu^*_\infty \mu^*_\infty}{U^*_\infty},$$

where ν^*_∞ is the far-field specific volume, while μ^*_∞ is the far-field dynamic viscosity. We refer to modes according to their temporal frequency and their spanwise wave number as (m, n), where m refers to the frequency $\omega_m = m\omega$ and n refers to the spanwise wave number $\beta_n = n\beta$.

A. High amplitude oblique-wave breakdown

It is well-known that NPSE can fail for sufficiently strong nonlinearities [8, 9], and this was demonstrated in an oblique-wave breakdown case presented in Joslin et al. (1993) [17]. The small amplitude case was studied using NOWNS in Sleeman et al. (2023) [14], and here we demonstrate that NOWNS is successful for the large amplitude case where NPSE fails. We note that oblique-wave breakdown has also been studied using both experiment and spatial DNS by Berlin et al. [19], while it was studied using NPSE for compressible flows by Chang and Malik [20]. We further note that whereas fundamental and subharmonic transition can be studied using Herbert's secondary stability theory [21], no such theory exists for oblique-wave breakdown, so that either experiment or numerical simulation is necessary to study this transition scenario [17, 19].

In this case, transition is initiated by two oblique waves with opposite wave angle, which are obtained from locally-parallel linear stability theory. The march starts at $\mathrm{Re}_x = 2.73529 \times 10^5$ with amplitude $u'^{(1,1)}_{\max}(x_0) = \sqrt{2} \times 10^{-2}$

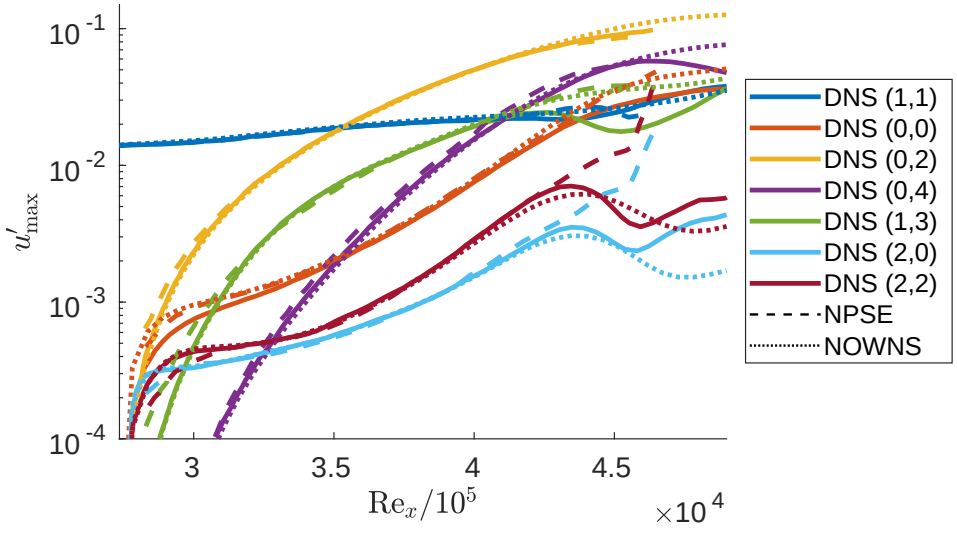

Fig. 1 Amplitude of u' v.s. streamwise coordinate, Re_x, for oblique-wave breakdown at frequency $F = 86\times10^{-6}$, spanwise wavenumber $b = 2/9\times10^{-3}$, with initial amplitude of $u'^{(1,1)}_{\max}(x_0) = \sqrt{2}\times10^{-2}$.

for all four waves, where we have defined the amplitudes

$$
\begin{aligned}
u'^{(0,0)}_{\max}(x) &= \max_y |u'_{0,0}(x,y)|,\\
u'^{(m,0)}_{\max}(x) &= \max_y \sqrt{2}|u'_{m,0}(x,y)|, \quad m = 1,\ldots,M,\\
u'^{(0,n)}_{\max}(x) &= \max_y \sqrt{2}|u'_{0,n}(x,y)|, \quad n = 1,\ldots,N,\\
u'^{(m,n)}_{\max}(x) &= \max_y 2\sqrt{2}|u'_{m,n}(x,y)|, \quad m = 1,\ldots,M, \quad n = 1,\ldots,N,
\end{aligned}
$$

to be consistent with the scaling used in [17]. The oblique waves interact to excite higher modes and to distort the mean flow. The grid extends over the domain $\mathrm{Re}_x \in [2.73529\times10^5, 4.9\times10^5]$ and $y \in [0, 60]$ with 2000 stations evenly spaced in x and 100 grid points in y, with the majority of the grid points clustered towards the wall, while the Fourier series is truncated at $M = 7$ temporal modes and $N = 7$ spanwise modes. We march downtream using the second-order backward differentiation formula (BDF2).

We consider the frequency $F = 86\times10^{-6}$ and the spanwise wavenumber $b = 2/9\times10^{-3}$ and we plot the amplitudes of the u-velocity as a function of streamwise station in figure 1. First we note that we have excellent agreement between the amplitudes predicted by NOWNS, NPSE, and DNS for the early stages of transition. However, NPSE begins to fail towards the end of the domain, while NOWNS is able to march all the way to the end of the DNS calculation. The DNS calculation is under-resolved near the end of the domain [17], which may explain the discrepancy between the DNS and NOWNS calculations. In figure 2, we plot the profiles for the u-velocity disturbances at the domain outlet for the vortex mode and the oblique wave. We observe that the maximum amplitude of the oblique wave occurs at $y = 2.55$, while the maximum amplitude of the vortex mode occurs at $y = 1.31$. In figures 3 and 4, we plot the contour the instantaneous contour of the u-velocity ($u = \boldsymbol{u} + u'$) as a function of the streamwise station and the spanwise coordinate, where figure 3 is plotted at $y = 2.55$ and figure 4 is plotted at $y = 1.31$. In figure 1, we observe that the oblique-wave, $(1, 1)$, is initially the dominant instability, but is rapidly overtaken by the vortex mode, $(0, 2)$, leading to the streaks observed in figures 3 and 4.

B. Oblique-wave breakdown with random noise

Next we demonstrate that NOWNS is robust to numerical noise. We consider the small-amplitude oblique-wave breakdown presented Joslin et al. (1993) [17], which we previously used to validate NOWNS [14]. We modify this test case such that we have the eigenfunction from the locally parallel linear stability theory, q_{LST}, and we add random noise,

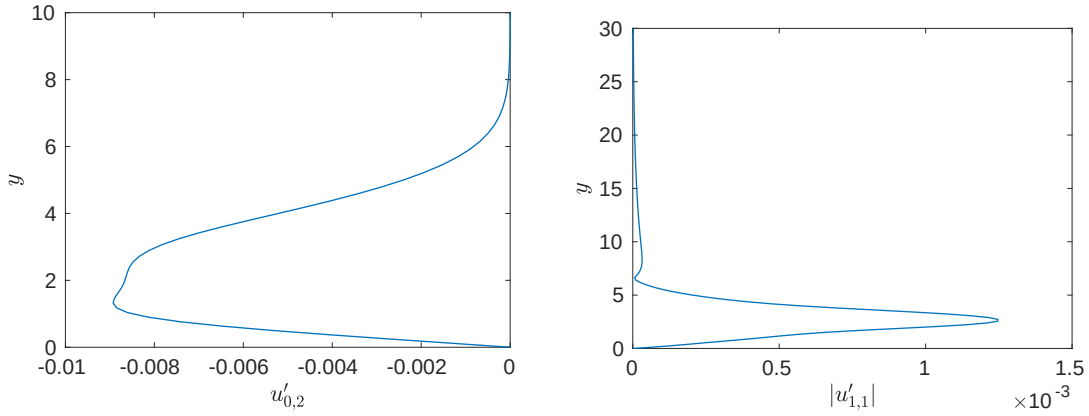

Fig. 2 Profiles of the u-velocity disturbances at $\mathrm{Re}_x = 4.9 \times 10^5$ for the vortex mode (left) and the oblique mode (right).

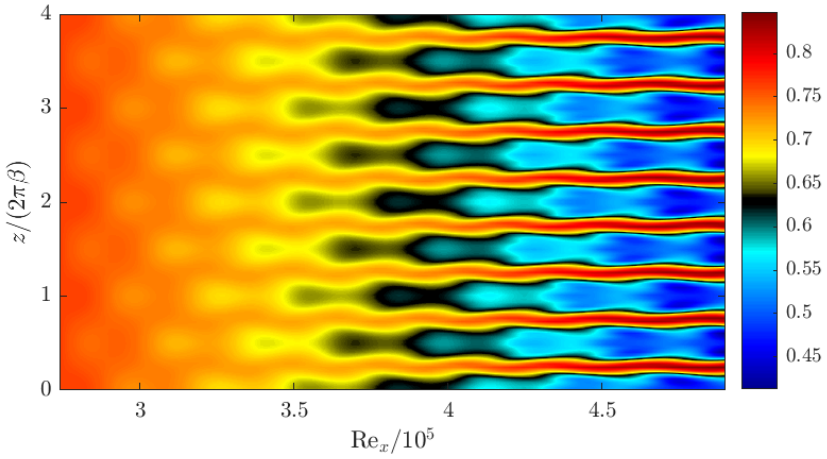

Fig. 3 Contour of the instantaneous u-velocity at for the large-amplitude oblique-wave breakdown case at $y = 2.55$, corresponding to the height at which the maximum amplitude of the oblique wave occurs.

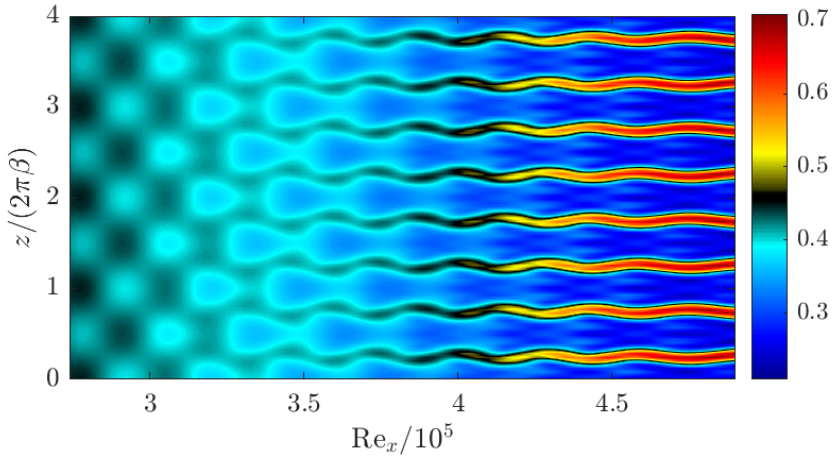

Fig. 4 Contour of the instantaneous u-velocity at for the large-amplitude oblique-wave breakdown case at $y = 1.31$, corresponding to the height at which the maximum amplitude of the vortex mode occurs.

q_{noise}, to obtain the inlet condition

$$q_{\text{LST}} + \varepsilon \tilde{q}_{\text{noise}}.$$

We choose complex random noise such that

$$\tilde{q}_{\text{noise}} = \tilde{q}_{\text{noise},r} + i\tilde{q}_{\text{noise},i}, \quad \tilde{q}_{\text{noise},r}, \tilde{q}_{\text{noise},i} \sim \mathcal{U}_{[-0.5,0.5]},$$

where $\mathcal{U}_{[a,b]}$ represents the uniform distribution over the interval $[a, b]$. We then normalize the noise to obtain q_{noise}, such that the maximum amplitude of the u-velocity noise is equal to the free-stream u-velocity, U_∞.

We start the march at $\mathrm{Re}_x = 2.73529 \times 10^5$, and with (small) amplitude $u'^{(1,1)}_{\text{max}} = \sqrt{2} \times 10^{-3}$, and we choose $\varepsilon = \sqrt{2} \times 10^{-6}$ to obtain the inlet conditions depicted in figures 5 and 6. The random noise does not perturb substantially the u- and w-velocities as shown in figure 5, and instead primarily perturbs the density and the pressure profiles as shown in figure 6. The grid extends over the domain $\mathrm{Re}_x \in [2.73529 \times 10^5, 6.084 \times 10^5]$ and $y \in [0, 60]$ with 2000 stations evenly spaced in x and 100 grid points in y, while the Fourier series is truncated at $M = 3$ temporal modes and $N = 4$ spanwise modes (we need fewer Fourier modes since we have a smaller disturbance). We also use the same frequency ($F = 86 \times 10^{-6}$) and spanwise wavenumber ($b = 2/9 \times 10^{-3}$) as the large amplitude case. We march the equations using the BDF2 scheme, and we find that the despite the noisy pressure and specific volume disturbances, the u-velocity amplitudes predicted by NOWNS for the noisy inlet condition agree closely with the amplitudes predicted by NOWNS for the inlet condition without noise, as depicted in figure 7. This figure also demonstrates that, although NPSE initially is able to accurately predict the evolution of the u-velocity amplitudes, it eventually becomes innaccurate (especially for $u'_{(0,0)}$ and $u'_{(2,0)}$) before failing to converge. On the other hand, NOWNS is able to accurately march downstream to the prescribed domain outlet. We additionally plot the u-velocity contour at $y = 2.55$ in figure 8. The perturbations for the small amplitude case are sufficiently small so that we do not observe the streak structures of the large amplitude case. Moreover, the noise introduced by the noisy inlet boundary condition does not affect substantially the u-velocity contour, so we plot only the case without noise.

We make this choice of for q_{noise} so that we can get a relatively small perturbation to the inlet boundary that causes the NPSE solver to fail, while still allowing the NOWNS march to be relatively accurate. By introducing relatively small perturbations to the u-velocity, and relatiely large perturbations to the specific volume and pressure, we can demonstrate that NOWNS can accurately evolve the u-velocity, despite the noise in the inlet boundary condition. If we introduce large perturbations to the u- and w-velocities, then the amplitude of the u- and w-velocity disturbance increase and we are no longer able to demonstrate good quantitative agreement with the noise-less inlet boundary condition (since the amplitude of the u-velocity is much larger).

To demonstrate the effect of the noisy inlet condition, we plot the contour of the real part of the u- and v-velocities of the oblique wave, with and without noise. In figure 9, we see that despite the noisy inlet condition, NOWNS evolves the

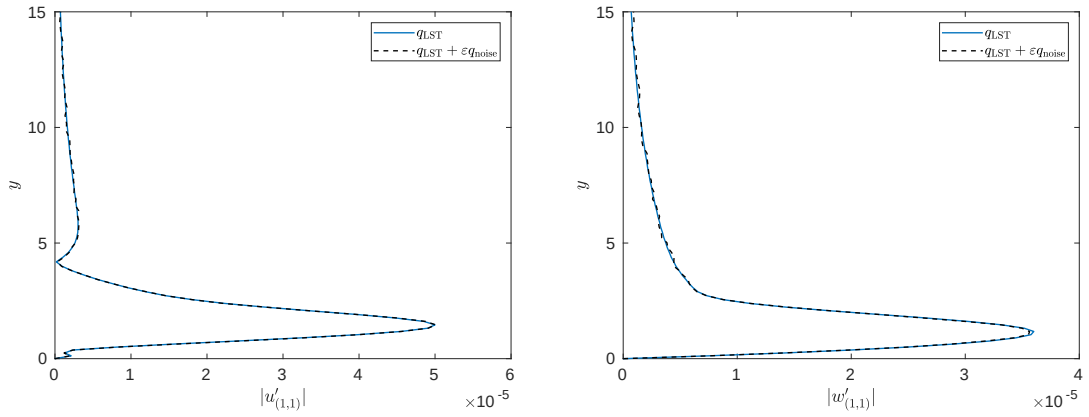

Fig. 5 Comparison of inlet boundary conditions with and without random noise (u-velocity and w-velocity).

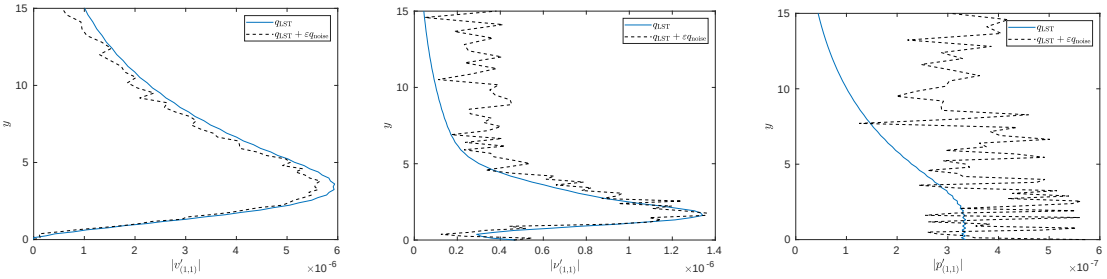

Fig. 6 Comparison of inlet boundary conditions with and without random noise (specific volume, v-velocity, and pressure).

u-velocity of the oblique wave such that it matches closely the case without noise. On the other hand, figure 10 shows that the v-velocity is more strongly affected by the numerical noise (the noise applied to the v-velocity is relatively large compared to the noise applied to the u-velocity), but we still qualitatively observe the same structures. The other modes (e.g., the vortex mode) are evolved accurately by the NOWNS calculation with noisy inlet condition, and the contour plots with and without the numerical noise are indistinguishable from each other, and so are not plotted here.

C. Blowing/suction strip

Blowing/suction strips are frequently used to study laminar-turbulent boundary layer transition in low-speed boundary layer flows [4, 5, 22–24]. For a flat-plate boundary layer flow, we specify no-slip boundary conditions such that

$$u(y = 0) = v(y = 0) = w(y = 0) = 0.$$

However, we can introduce disturbances through a blowing/suction strip by specifying a non-zero wall-normal velocity such that $v(y = 0) = f(x, z, t)$, for some function $f(x, z, t)$ that is periodic in t and z. NPSE does not support blowing/suction strips because they introduce non-modal disturbances. The NOWNS approach is advantageous because it supports non-modal intstabilities, and we demonstrate here that NOWNS supports blowing-suctions strips.

Rist et al. (1995) used a blowing/suction strip to study K-type (fundamental) transition using DNS. A similar study was performed using DNS by Sayadi et al. (2013) [22], and using a harmonic balance method (HBM) by Rigas et al. (2021) [24]. The blowing/suction strip is given by

$$f(x, z, t) = 5 \times 10^{-3} \sin(\omega t) v_a(x) + 1.3 \times 10^{-4} \cos(\beta z) v_s(x), \tag{19}$$

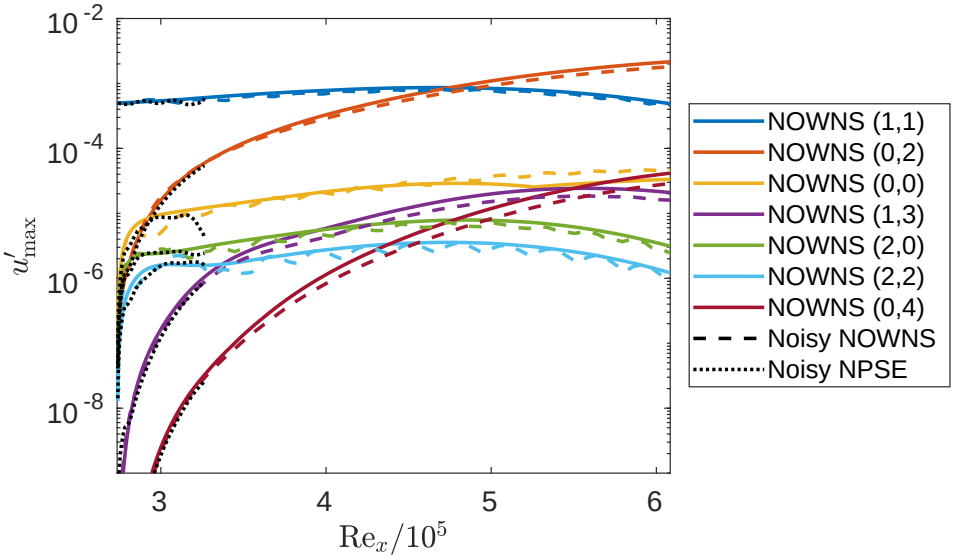

Fig. 7 Amplitude of u' v.s. streamwise coordinate, Re_x, for oblique-wave breakdown at frequency $F = 86 \times 10^{-6}$, spanwise wavenumber $b = 2/9 \times 10^{-3}$, with initial amplitude of $u'^{(1,1)}_{\max}(x_0) = \sqrt{2} \times 10^{-3}$ with and without random noise.

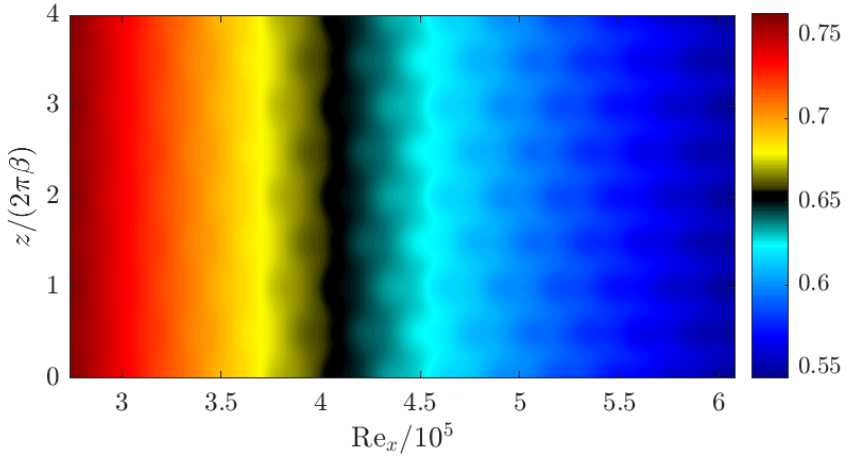

Fig. 8 Contour of the instantaneous u-velocity at for the small-amplitude oblique-wave breakdown case at $y = 2.55$.

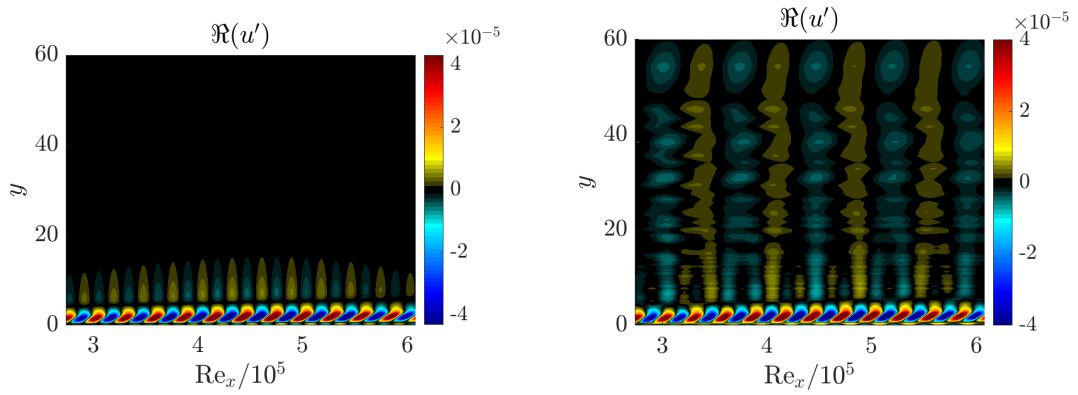

Fig. 9 Contour plot of the real part of $u_{(1,1)}$ with and without numerical noise, for the small-amplitude oblique wave breakdown case.

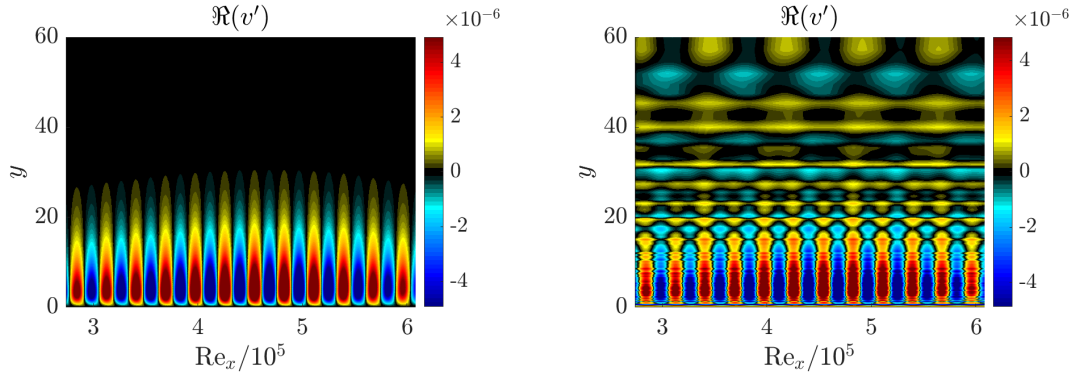

Fig. 10 Contour plot of the real part of $v_{(1,1)}$ with and without numerical noise, for the small-amplitude oblique wave breakdown case.

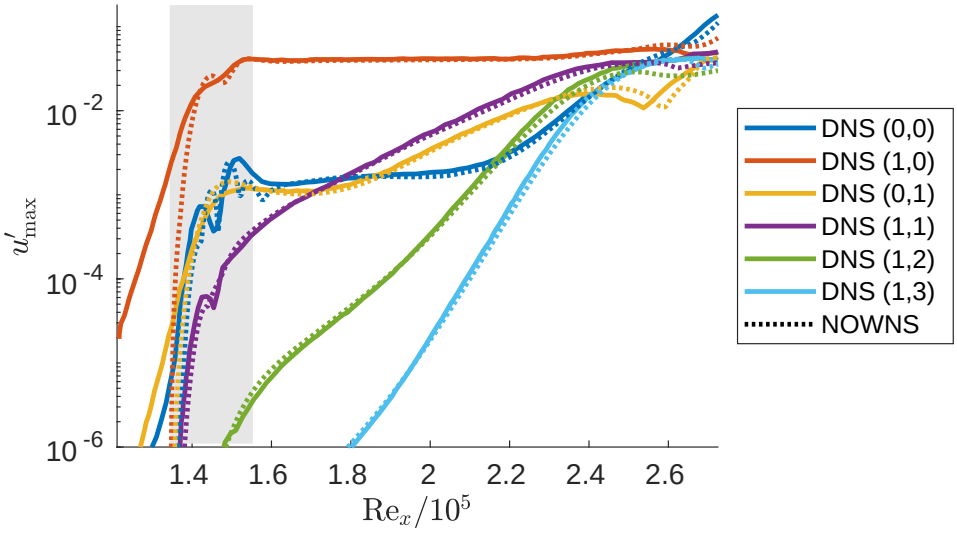

Fig. 11 Amplitude of u' v.s. streamwise coordinate, Re_x, for fundamental breakdown at frequency $F = 110\times10^{-6}$, spanwise wavenumber $b = 0.423\times10^{-3}$, with blowing and suction

where

$$v_a(\mathrm{Re}_x) = \begin{cases} 0, & \mathrm{Re}_x \le \mathrm{Re}_x(x_1) \\ 15.1875\xi^5 - 35.4375\xi^4 + 20.25\xi^3, & \mathrm{Re}_x(x_1) < \mathrm{Re}_x \le \mathrm{Re}_x(x_m) \\ -v_a\big(2\mathrm{Re}_x(x_m) - \mathrm{Re}_x\big), & \mathrm{Re}_x(x_m) < \mathrm{Re}_x \le \mathrm{Re}_x(x_2) \\ 0, & \mathrm{Re}_x(x_2) < \mathrm{Re}_x \end{cases} \tag{20a}$$

$$v_s(\mathrm{Re}_x) = \begin{cases} 0, & R \le \mathrm{Re}_x(x_1) \\ -3\xi^4 + 4\xi^3, & \mathrm{Re}_x(x_1) < \mathrm{Re}_x \le \mathrm{Re}_x(x_m) \\ v_s\big(2\mathrm{Re}_x(x_m) - \mathrm{Re}_x\big), & \mathrm{Re}_x(x_m) < \mathrm{Re}_x \le \mathrm{Re}_x(x_2) \\ 0, & \mathrm{Re}_x(x_2) < \mathrm{Re}_x \end{cases} \tag{20b}$$

for $\mathrm{Re}_x(x_1) = 1.3438\times10^5$, $\mathrm{Re}_x(x_2) = 1.5532\times10^5$, $x_m = (x_1+x_2)/2$, and $\xi = (\mathrm{Re}_x - \mathrm{Re}_x(x_1))/(\mathrm{Re}_x(x_m) - \mathrm{Re}_x(x_1))$. The frequency is chosen to be $F = 110\times10^{-6}$ with spanwise wavenumber $b = 0.423\times10^{-3}$. We integrate over the streamwise domain $\mathrm{Re}_x \in [1.33956\times10^5, 2.72\times10^5]$ with $y \in [0, 60]$, where we have 1300 stations in x and 100 grid points in y, while we have $M = 4$ temporal modes and $N =$ spanwise modes. We plot the ampliutdes of the u-velocity in figure 11, and we see that we have good agreement between the NOWNS and DNS of Rist et al. (1995) [5]. We note that in the early stages of the march there is disagreement between the DNS and NOWNS calculations because the blowing/suction strip causes upstream effects that NOWNS neglects by construction. Whereas for the DNS calculation, the modes have a non-zero amplitude upstream of the blowing/suction strip, the amplitudes in the NOWNS calculation initially have zero amplitude at the first blowing/suction strip station. However, boundary-layer flows involve convective instabilities that convect downstream with the flow, and the amplitudes predicted by NOWNS quickly converge to those predicted by DNS as the march moves downstream.

IV. Conclusions and future work

The NOWNS procedure was first outlined by Sleeman et al. (2023) [14] and it was demonstrated that NOWNS is successful for cases where NPSE can be applied with a lower computational cost. The present work demonstrates that NOWNS is successful in cases where NPSE fails. In particular, we have shown that NOWNS supports higher amplitude disturbances, is robust to random noise, and supports a blowing-suction strip. In the future, we would like to apply NOWNS to study H-type (subharmonic) and K-type (fundamental) transition. H- and K-type transition has been studied experimentally [25, 26], theoretically using secondary stability theory [21], and numerically using NPSE [27],

DNS [4, 5, 22], large eddy simulation (LES) [23] and a Harmonic Balance Method (HBM) [24]. We also further study the oblique-wave breakdown case and compare our NOWNS results to the experimental and DNS results of Berlin et al. (1999) [19]. Linear OWNS has previously been used to study laminar-turbulent transition in high-speed boundary-layer flows [11], so we additionally plan to extend the NOWNS framework to support high-speed flows.

V. Appendices

A. Linearized Navier-Stokes Operators

Here we present the operators for the Navier-Stokes equations. The operators for the first derivatives, A, B_y, and B_z, are given by

$$A(\boldsymbol{q}) = \begin{bmatrix} u & -\nu & 0 & 0 & 0 \\ 0 & u & 0 & 0 & 0 \\ 0 & 0 & u & 0 & 0 \\ 0 & 0 & 0 & u & 0 \\ 0 & \gamma p & 0 & 0 & u \end{bmatrix}, \quad B_y(\boldsymbol{q}) = \begin{bmatrix} v & 0 & -\nu & 0 & 0 \\ 0 & v & 0 & 0 & 0 \\ 0 & 0 & v & 0 & 0 \\ 0 & 0 & 0 & v & 0 \\ 0 & 0 & \gamma p & 0 & v \end{bmatrix}, \quad B_z(\boldsymbol{q}) = \begin{bmatrix} w & 0 & 0 & -\nu & 0 \\ 0 & w & 0 & 0 & 0 \\ 0 & 0 & w & 0 & 0 \\ 0 & 0 & 0 & w & 0 \\ 0 & 0 & 0 & \gamma p & w \end{bmatrix},$$

while the operator for the second derivative, B_2, is given by

$$B_2(\boldsymbol{q}) = \begin{bmatrix} 0 & 0 & 0 & 0 & 0 \\ 0 & -\frac{\nu}{Re} & 0 & 0 & 0 \\ 0 & 0 & -\frac{\nu}{Re} & 0 & 0 \\ 0 & 0 & 0 & -\frac{\nu}{Re} & 0 \\ -\frac{\gamma p}{RePr} & 0 & 0 & 0 & -\frac{\gamma \nu}{RePr} \end{bmatrix}.$$

Finally, the operator C that we get using the Reynolds decomposition is given by

$$C(\boldsymbol{q}) = \begin{bmatrix} -\nabla \cdot \boldsymbol{u} & \frac{\partial \nu}{\partial x} & \frac{\partial \nu}{\partial y} & \frac{\partial \nu}{\partial z} & 0 \\ \frac{\partial p}{\partial x} - \frac{1}{Re}\nabla^2 u & \frac{\partial u}{\partial x} & \frac{\partial u}{\partial y} & \frac{\partial u}{\partial z} & 0 \\ \frac{\partial p}{\partial y} - \frac{1}{Re}\nabla^2 v & \frac{\partial v}{\partial x} & \frac{\partial v}{\partial y} & \frac{\partial v}{\partial z} & 0 \\ \frac{\partial p}{\partial z} - \frac{1}{Re}\nabla^2 w & \frac{\partial w}{\partial x} & \frac{\partial w}{\partial y} & \frac{\partial w}{\partial z} & 0 \\ -\frac{\gamma}{RePr}\nabla^2 p & \frac{\partial p}{\partial x} & \frac{\partial p}{\partial y} & \frac{\partial p}{\partial z} & \gamma \nabla \cdot \boldsymbol{u} - \frac{\gamma}{RePr}\nabla^2 \nu \end{bmatrix}.$$

B. Parabolization using the OWNS projection procedure

The eigenvalues of $A(\bar{\boldsymbol{q}})$ determine which modes are upstream- and downstream-going. Therefore, is helpful, but not necessary, to transform to characteristic variables (based on the eigen-decomposition of $A(\bar{\boldsymbol{q}})$) to derive the OWNS parabolization procedure. The eigen-decomposition of $A(\bar{\boldsymbol{q}})$ is known analytically, with eigenvectors $T(\bar{\boldsymbol{q}})$ and eigenvalues

$$\tilde{A}(\bar{\boldsymbol{q}}) = T(\bar{\boldsymbol{q}})A(\bar{\boldsymbol{q}})T^{-1}(\bar{\boldsymbol{q}}), \tag{21}$$

We define the disturbance in the characteristic variables

$$\boldsymbol{\phi}(x, y, z, t) = T(\bar{\boldsymbol{q}})\boldsymbol{q}'(x, y, z, t), \tag{22}$$

which we will use to parabolize our stability equations. From now on, we drop the argument to T and assume that it is evaluated at $\bar{\boldsymbol{q}}$. To transform our equation to characteristic variables, we pre-multiply by T and use $\boldsymbol{q}' = T^{-1}\boldsymbol{\phi}$ to obtain

$$TA(\bar{\boldsymbol{q}})\frac{\partial (T^{-1}\boldsymbol{\phi})}{\partial x} = TL(\bar{\boldsymbol{q}})T^{-1}\boldsymbol{\phi} + T\boldsymbol{f}. \tag{23}$$

Using the streamwise derivative

$$\frac{\partial (T^{-1}\boldsymbol{\phi})}{\partial x} = \frac{\partial T^{-1}}{\partial x}\boldsymbol{\phi} + T^{-1}\frac{\partial \boldsymbol{\phi}}{\partial x},$$

we define the linear operator and the forcing function in characteristic variables

$$\tilde{L}(\bar{\boldsymbol{q}}) = TL(\bar{\boldsymbol{q}})T^{-1} - TA(\bar{\boldsymbol{q}})\frac{\partial T^{-1}}{\partial x}, \tag{24a}$$

$$\tilde{\boldsymbol{f}} = T\boldsymbol{f}, \tag{24b}$$

which results in

$$\tilde{A}(\bar{\boldsymbol{q}})\frac{\partial \boldsymbol{\phi}}{\partial x} = \tilde{L}(\bar{\boldsymbol{q}})\boldsymbol{\phi} + \tilde{\boldsymbol{f}}. \tag{25}$$

This equation still supports both upstream- and downtream-going modes, so we will now outline how to remove the upstream effects.

The OWNS projection (OWNS-P) [15] supports inhomogeneous equations of the form (25), while the OWNS outflow (OWNS-O) supports only homogeneous equations of the form [28]. The nonlinear terms in NOWNS can be treated as a forcing function, so we will consider only the OWNS-P approach. Throughout this section, we drop the argument $\bar{\boldsymbol{q}}$ to our linear operators for brevity. First we note that the diagonal matrix $\tilde{A}$ can be re-organized as

$$\tilde{A} = \begin{bmatrix} \tilde{A}_{++} & 0 & 0 \\ 0 & \tilde{A}_{--} & 0 \\ 0 & 0 & \tilde{A}_{00} \end{bmatrix}, \tag{26}$$

for the N_+ positive eigenvalues $\tilde{A}_{++}$, the N_- negative eigenvalues $\tilde{A}_{--}$, and the N_0 zero eigenvalues $\tilde{A}_{00} = 0$. We can further define

$$\tilde{A}_{\pm\pm} = \begin{bmatrix} \tilde{A}_{++} & 0 \\ 0 & \tilde{A}_{--} \end{bmatrix}, \quad \tilde{L}_{\pm\pm} = \begin{bmatrix} \tilde{L}_{++} & \tilde{L}_{+-} \\ \tilde{L}_{-+} & \tilde{L}_{--} \end{bmatrix}, \quad \tilde{L}_{\pm 0} = \begin{bmatrix} \tilde{L}_{+0} \\ \tilde{L}_{-0} \end{bmatrix}, \tag{27}$$

and

$$\boldsymbol{\phi} = \begin{bmatrix} \boldsymbol{\phi}_\pm \\ \boldsymbol{\phi}_0 \end{bmatrix}, \quad \tilde{\boldsymbol{f}} = \begin{bmatrix} \tilde{\boldsymbol{f}}_\pm \\ \tilde{\boldsymbol{f}}_0 \end{bmatrix}, \tag{28}$$

so that our equations become

$$\tilde{A}_{\pm\pm}\frac{\partial \boldsymbol{\phi}_\pm}{\partial x} = \tilde{L}_{\pm\pm}\boldsymbol{\phi}_\pm + \tilde{L}_{\pm 0}\boldsymbol{\phi}_0 + \boldsymbol{f}_\pm, \tag{29a}$$

$$0 = \tilde{L}_{0\pm}\boldsymbol{\phi}_\pm + \tilde{L}_{00}\boldsymbol{\phi}_0 + \boldsymbol{f}_0, \tag{29b}$$

which is a differential algebraic equation (DAE) of index 1. We can use the algebraic constraint (29b) to obtain

$$\boldsymbol{\phi}_0 = -\tilde{L}_{00}^{-1}[\tilde{L}_{0\pm}\boldsymbol{\phi}_\pm + \boldsymbol{f}_0], \tag{30}$$

and we define

$$M = \tilde{A}_{\pm\pm}^{-1}[\tilde{L}_{\pm\pm} - \tilde{L}_{\pm 0}\tilde{L}_{00}^{-1}\tilde{L}_{0\pm}], \tag{31a}$$

$$\boldsymbol{g} = \tilde{A}_{\pm\pm}^{-1}[\tilde{\boldsymbol{f}}_\pm - \tilde{L}_{\pm 0}L_{00}^{-1}\tilde{\boldsymbol{f}}_0], \tag{31b}$$

so that our DAE can be written as the ODE

$$\frac{\partial \boldsymbol{\phi}_\pm}{\partial x} = M\boldsymbol{\phi}_\pm + \boldsymbol{g}. \tag{32}$$

The upstream- and downstream-going modes of (32) can be determined based on the eigenvalues of M, according to Brigg's criterion [28, 29], which can then be used to introduce well-posed one-way equations, according to the criterion of Kreiss [30].

The linear operator M has the eigen-decomposition $M = VDV^{-1}$ and the solution $\boldsymbol{\phi}_\pm$ can be expanded as a linear combination of V

$$\boldsymbol{\phi}_\pm = V\boldsymbol{\psi} = \sum_{k=1}^{N} \boldsymbol{v}^{(k)}\psi_k,$$

From Brigg's criterion, we know that M has N_+ upstream- and N_- downstream-going modes. Therefore, we can further partition V into its downstream- (V_+) and upstream-going (V_-) components so that

$$\boldsymbol{\phi}_\pm = V\boldsymbol{\psi} = \begin{bmatrix} V_+ & V_- \end{bmatrix} \begin{bmatrix} \boldsymbol{\psi}_+ \\ \boldsymbol{\psi}_- \end{bmatrix},$$

with the eigenvalues

$$D = \begin{bmatrix} D_{++} & 0 \\ 0 & D_{--} \end{bmatrix}.$$

We use the eigensystem of M to define a projection operator

$$P = V \begin{bmatrix} I_{++} & 0 \\ 0 & 0 \end{bmatrix} V^{-1},$$

which retains the downstream-going modes associated with $\boldsymbol{\psi}_+$ while removing the upstream-going modes associated with $\boldsymbol{\psi}_-$ such that

$$\boldsymbol{\phi}'_\pm = P\boldsymbol{\phi}_\pm, \quad \boldsymbol{\phi}''_\pm = [I - P]\boldsymbol{\phi}_\pm.$$

Explicitly using Brigg's criterion to identify upstream- and downstream-going modes in a rigorous way would be computationally expensive, so we instead apply the projection operator approximately using a recursive filter [15, 28]. However, to simplify the exposition, we will delay the discussion of the approximate projection operator until section V.B.1.

We use linearity to assert that

$$\frac{\partial \boldsymbol{\phi}'_\pm}{\partial x} + \frac{\partial \boldsymbol{\phi}''_\pm}{\partial x} = P[M\boldsymbol{\phi}_\pm + \boldsymbol{g}] + [I - P][M\boldsymbol{\phi}_\pm + \boldsymbol{g}],$$

and it is shown in [15] that P and M commute so that

$$\begin{aligned} PM\boldsymbol{\phi}_\pm &= MP\boldsymbol{\phi}_\pm = M\boldsymbol{\phi}'_\pm, \\ [I - P]M\boldsymbol{\phi}_\pm &= M[I - P]\boldsymbol{\phi}_\pm = M\boldsymbol{\phi}''_\pm. \end{aligned}$$

The equations can be split in two

$$\frac{\partial \boldsymbol{\phi}'_\pm}{\partial x} = M\boldsymbol{\phi}'_\pm + P\boldsymbol{g}, \tag{33a}$$

$$\frac{\partial \boldsymbol{\phi}''_\pm}{\partial x} = M\boldsymbol{\phi}''_\pm + [I - P]\boldsymbol{g}, \tag{33b}$$

so that we can solve two one-way equations to recover the full elliptic solution as

$$\boldsymbol{\phi}'_\pm + \boldsymbol{\phi}''_\pm = P\boldsymbol{\phi}_\pm + [I - P]\boldsymbol{\phi}_\pm = \boldsymbol{\phi}_\pm.$$

It was demonstrated in [15] that two one-way equations can be solved to recover the full two-way solution.

1. Approximate projection operator

It is computationally expensive to construct the exact projection operator, so we will apply it approximately using the recursive filter approach described in [15]. It is shown in [15] that applying the following equations

$$\boldsymbol{\phi}_+^{(-N_b)} = 0 \tag{34a}$$

$$(M - i\beta_-^{(j)} I_\pm)\boldsymbol{\phi}_\pm^{(-j)} - (M - i\beta_+^{(j)} I_\pm)\boldsymbol{\phi}_\pm^{(-j-1)} = 0, \quad j = 1, \ldots, N_b - 1 \tag{34b}$$

$$(M - i\beta_-^{(0)} I_\pm)\boldsymbol{\phi}_\pm^{(0)} - (M - i\beta_+^{(0)} I_\pm)\boldsymbol{\phi}_\pm^{(-1)} = (M - i\beta_-^{(0)} I_\pm)\boldsymbol{\phi}_\pm \tag{34c}$$

$$(M - i\beta_+^{(j)} I_\pm)\boldsymbol{\phi}_\pm^{(j)} - (M - i\beta_-^{(j)} I_\pm)\boldsymbol{\phi}_\pm^{(j+1)} = 0, \quad j = 0, \ldots, N_b - 1 \tag{34d}$$

$$\boldsymbol{\phi}_-^{(N_b)} = 0, \tag{34e}$$

to the elliptic variable $\boldsymbol{\phi}_\pm$ results in the parabolic variable $\boldsymbol{\phi}_\pm^{(0)}$. Then we use the algebraic constraint (29b) to obtain $\boldsymbol{\phi}_0$. Here, $\{\beta_\pm^{(j)}\}_{j=0}^{N_b-1}$ are termed the *recursion parameters*, while $\{\boldsymbol{\phi}^{(j)}\}_{j=-N_b}^{N_b}$ are termed the *auxiliary variables*. Finally, the projection operator can also be applied approximately using the OWNS recursive (OWNS-R) approach [31], which entails a lower computational cost than OWNS-P. However, we prefer the OWNS-P approach because we have found it to be more robust.

2. Approximate projection operator applied to equations

We have demonstrated how to apply the approximate projection operator to our disturbance variable, but we also wish to apply it to our equations. We wish to solve the equation

$$\frac{\partial \boldsymbol{\phi}'_\pm}{\partial x} = P[M\boldsymbol{\phi}'_\pm + \boldsymbol{g}], \tag{35}$$

using our approximate projection operator. First we note that this is equivalent to

$$\frac{\partial \boldsymbol{\phi}'_\pm}{\partial x} = P\tilde{A}_{\pm\pm}^{-1}[\tilde{L}_{\pm\pm}\boldsymbol{\phi}'_\pm + \tilde{L}_{\pm 0}\boldsymbol{\phi}'_0 + \tilde{\boldsymbol{f}}_\pm], \tag{36a}$$

$$0 = \tilde{L}_{0\pm}\boldsymbol{\phi}'_\pm + \tilde{L}_{00}\boldsymbol{\phi}'_0 + \tilde{\boldsymbol{f}}_0, \tag{36b}$$

and then we define the residual

$$\boldsymbol{r}_\pm(\boldsymbol{\phi}) = \tilde{A}_{\pm\pm}^{-1}[\tilde{L}_{\pm\pm}\boldsymbol{\phi}_\pm + \tilde{L}_{\pm 0}\boldsymbol{\phi}_0 + \tilde{\boldsymbol{f}}_\pm], \tag{37a}$$

$$\boldsymbol{r}_0(\boldsymbol{\phi}) = \tilde{L}_{0\pm}\boldsymbol{\phi}_\pm + \tilde{L}_{00}\boldsymbol{\phi}_0 + \tilde{\boldsymbol{f}}_0, \tag{37b}$$

so that

$$\frac{\partial \boldsymbol{\phi}'_\pm}{\partial x} = P\boldsymbol{r}_\pm(\boldsymbol{\phi}'), \tag{38a}$$

$$0 = \boldsymbol{r}_0(\boldsymbol{\phi}'). \tag{38b}$$

Then we apply the recursive filter to $\boldsymbol{r}_\pm(\boldsymbol{\phi}')$ as

$$\boldsymbol{r}_+^{(-N_b)} = 0 \tag{39a}$$

$$(M - i\beta_-^{(j)}I_\pm)\boldsymbol{r}_\pm^{(-j)} - (M - i\beta_+^{(j)}I_\pm)\boldsymbol{r}_\pm^{(-j-1)} = 0, \quad j = 1, \ldots, N_b - 1 \tag{39b}$$

$$(M - i\beta_-^{(0)}I_\pm)\boldsymbol{r}_\pm^{(0)} - (M - i\beta_+^{(0)}I_\pm)\boldsymbol{r}_\pm^{(-1)} = (M - i\beta_-^{(0)}I_\pm)\boldsymbol{r}_\pm \tag{39c}$$

$$(M - i\beta_+^{(j)}I_\pm)\boldsymbol{r}_\pm^{(j)} - (M - i\beta_-^{(j)}I_\pm)\boldsymbol{r}_\pm^{(j+1)} = 0, \quad j = 0, \ldots, N_b - 1 \tag{39d}$$

$$\boldsymbol{r}_-^{(N_b)} = 0. \tag{39e}$$

Alternatively, we can expand this filter to include $\boldsymbol{r}_0(\boldsymbol{\phi}')$ as

$$\boldsymbol{r}_+^{(-N_b)} = 0 \tag{40a}$$

$$(\tilde{L} - i\beta_-^{(j)}\tilde{A})\boldsymbol{r}^{(-j)} - (\tilde{L} - i\beta_+^{(j)}\tilde{A})\boldsymbol{r}^{(-j-1)} = 0, \quad j = 1, \ldots, N_b - 1 \tag{40b}$$

$$(\tilde{L} - i\beta_-^{(0)}\tilde{A})\boldsymbol{r}^{(0)} - (\tilde{L} - i\beta_+^{(0)}\tilde{A})\boldsymbol{r}^{(-1)} = (\tilde{L} - i\beta_-^{(0)}\tilde{A})\boldsymbol{r} \tag{40c}$$

$$(\tilde{L} - i\beta_+^{(j)}\tilde{A})\boldsymbol{r}^{(j)} - (\tilde{L} - i\beta_-^{(j)}\tilde{A})\boldsymbol{r}^{(j+1)} = 0, \quad j = 0, \ldots, N_b - 1 \tag{40d}$$

$$\boldsymbol{r}_-^{(N_b)} = 0, \tag{40e}$$

with the additional constraint

$$\boldsymbol{r}_0^{(0)} = \boldsymbol{r}_0, \tag{40f}$$

where we should have $\boldsymbol{r}_0 = 0$. We introduce the auxiliary variables

$$\boldsymbol{\phi}_{\text{aux}} = \begin{bmatrix} \boldsymbol{r}_+^{(-N_b)} \\ \boldsymbol{r}^{(-N_b+1)} \\ \vdots \\ \boldsymbol{r}^{(-1)} \\ \boldsymbol{r}^{(0)} \\ \boldsymbol{r}^{(1)} \\ \vdots \\ \boldsymbol{r}^{(N_b-1)} \\ \boldsymbol{r}_-^{(N_b)} \end{bmatrix}, \tag{41}$$

and the operators P_1 and P_2, where $P_1\boldsymbol{r}$ gives the right-hand-side of (40), while $P_2\boldsymbol{\phi}_{\text{aux}}$ gives the left-hand-side. Then, we extract $\boldsymbol{r}_\pm^{(0)}$ from $\boldsymbol{\phi}_{\text{aux}}$ as $\boldsymbol{r}_\pm^{(0)} = P_3\boldsymbol{\phi}_{\text{aux}}$. The action of the approximate projection operator on the equations can be expressed compactly as

$$\boldsymbol{r}_\pm^{(0)} = P_3\boldsymbol{\phi}_{\text{aux}}, \tag{42a}$$
$$P_2\boldsymbol{\phi}_{\text{aux}} = P_1\boldsymbol{r}, \tag{42b}$$

which allows us to write our equations as

$$\frac{\partial \boldsymbol{\phi}'_\pm}{\partial x} = P_3\boldsymbol{\phi}_{\text{aux}} \tag{43a}$$
$$P_2\boldsymbol{\phi}_{\text{aux}} = P_1\boldsymbol{r}_\pm(\boldsymbol{\phi}'), \tag{43b}$$
$$0 = \boldsymbol{r}_0(\boldsymbol{\phi}'), \tag{43c}$$

or

$$\frac{\partial \boldsymbol{\phi}'_\pm}{\partial x} = P_3\boldsymbol{\phi}_{\text{aux}}, \tag{44a}$$
$$P_2\boldsymbol{\phi}_{\text{aux}} = P_1\tilde{A}_{\pm\pm}^{-1}[\tilde{L}_{\pm\pm}\boldsymbol{\phi}'_\pm + \tilde{L}_{\pm 0}\boldsymbol{\phi}'_0 + \tilde{\boldsymbol{f}}_\pm], \tag{44b}$$
$$0 = \tilde{L}_{0\pm}\boldsymbol{\phi}'_\pm + \tilde{L}_{00}\boldsymbol{\phi}'_0 + \tilde{\boldsymbol{f}}_0. \tag{44c}$$

We note that if $\boldsymbol{r}_0(\boldsymbol{\phi}') = 0$, then we will have the constraint $\boldsymbol{r}_0^{(0)} = 0$.

C. Recursion parameter sets

The recursion parameters are chosen based on the eigenvalues of the Euler equations linearized about a uniform flow, as described in [28]. The eigenvalues are

$$i\alpha_c = \frac{ik}{\bar{M}_x}, \quad i\alpha_{a_1}(z) = ik\frac{-\bar{M}_x + \mu(z)}{1-\bar{M}_x^2}, \quad i\alpha_{a_2}(z) = ik\frac{-\bar{M}_x - \mu(z)}{1-\bar{M}_x^2},$$

where $\bar{M}_x = \bar{u}/\bar{c}$ is the local streamwise Mach number, $k = \omega/\bar{c}$ is the streamwise wave number, z is a composite wave-number (for the transverse directions), and the function $\mu(z)$ is given by

$$\mu(z) = \sqrt{1-(1-\bar{M}_x^2)z^2}.$$

For subsonic boundary layer flows, we use the same recursion parameters as in [10], which differ slightly from those developed originally in [28], so we will briefly explain the new choice of recursion parameters.

The present choice of recursion parameters are separated into the following groups: (i) vortical modes, which replace convective modes, (ii) fast and slow stream evanescent acoustic modes, and (iii) fast and slow stream propagating acoustic modes, where fast stream modes are associated with the free-stream streamwise Mach number, while slow

stream modes are associated with a small Mach number (inside the boundary layer). The recursion parameters for the vortical modes of the present study match closely the parameters for convective modes in [28], while the recursion parameters for the propagating acoustic modes are distributed the same way in both the present study and in [28]. The parameters for the evanescent acoustic modes are distributed in a slightly different way, so we focus our discussion on these parameters.

To distribute the parameters for the evanescent acoustic modes, we define

$$\eta_c = \frac{k}{1-\bar{M}_x}, \quad \eta_m = 1.5\frac{L_y}{\Delta y},$$

where L_y is the (dimensionless) extent of the domain in the wall-normal direction, while Δy is the (uniform) wall-normal grid-spacing. These define the spacing parameter

$$\eta^{(h)} = \eta_m + \frac{h}{N_e - 1}\Big(\eta_c + 0.1\frac{\eta_m - \eta_c}{N_e - 1} - \eta_m\Big), \quad h = 0, \ldots, N_e - 1,$$

which in turn defines

$$\mu^{(h)} = \mu(\eta^{(h)}), \quad h = 0, \ldots, N_e - 1.$$

This contrasts with the choice

$$\mu^{(h)} = \mu_{\max}\frac{h}{2N_e}, \quad h = 0, \ldots, 2N_e - 1,$$

used in [28], where $\mu_{\max} = \mu(z_{\max})$. Here, $z_{\max}$ represents the maximum transverse wave number supported by the semi-discrete Euler equations (wave numbers larger than $z_{\max}$ need not be considered because they are not supported by the semi-discrete equations). The present approach considers a range of z near $z_{\max}$ (distributed according to $\eta^{(h)}$) which is then used to define $\mu^{(h)}$, while the approach presented in [28] considers only one z to get $\mu_{\max}$, which is then used to define $\mu^{(h)}$ spaced linearly over $[0, \mu_{\max}]$. The present approach is advantageous because $\mu(z)$ is nonlinear in z.

The recursion parameter sets for a subsonic boundary layer flow are summarized in table 1. The fast-stream values are denoted k_1 and $\bar{M}_{x,1}$, while the slow-stream values are denoted k_2 and $\bar{M}_{x,2}$. The acoustic modes must be computed for both the fast- and slow-stream values.

Type	Spacing	$\beta_+^{(j)}$	$\beta_-^{(j)}$
Vortical	$b^{(h)} = \frac{k_1}{\bar{M}_{x,1}} + \frac{h}{N_\omega}\left(\frac{k_2}{\bar{M}_{x,2}} - \frac{k_1}{\bar{M}_{x,1}}\right)$ $h = 0, \ldots, N_\omega - 1$	$(1+i)b^{(j)}$	$\frac{-2k_2M_2}{1-M_2^2} - b^{(j)}$
Evanescent acoustic	$\mu^{(h)} = \sqrt{k^2 - (1-\bar{M}_x^2)(\eta^{(h)})^2}$ $h = 0, \ldots, N_e - 1$	$\frac{-\bar{M}_x k + \mu^{(j)}}{1-\bar{M}_x^2}$	$\frac{-\bar{M}_x k - \mu^{(j)}}{1-\bar{M}_x^2}$
Propagating acoustic	$\theta^{(h)} = \frac{h}{N_p}\pi/2$ $h = 0, \ldots, 2N_p - 1$	$k\frac{-\bar{M}_x + \cos\theta^{(2j)}}{1-\bar{M}_x^2}$	$k\frac{-\bar{M}_x - \cos\theta^{(2j+1)}}{1-\bar{M}_x^2}$

Table 1 Recursion parameter sets for subsonic boundary layer flows.

Acknowledgments

This work has been supported by The Boeing Company through the Strategic Research and Development Relationship Agreement CT-BA-GTA-1.

References

[1] Smith, A., Company, D. A., Gamberoni, N., Sub-Committee, A. R. C. F. M., and Department, D. A. C. E. S. D. E., *Transition, Pressure Gradient and Stability Theory*, ARC-19322, Douglas Aircraft Company, El Segundo Division, 1956.

[2] Van Ingen, J., Sub-Committee, A. R. C. F. M., and Technische Hogeschool Delft, V., *A Suggested Semi-empirical Method for the Calculation of the Boundary Layer Transition Region*, ARC-19337, TH Delft, Delft, 1956.

[3] Crouch, J. D., and Ng, L. L., "Variable N-Factor Method for Transition Prediction in Three-Dimensional Boundary Layers," *AIAA Journal*, Vol. 38, No. 2, 2000, pp. 211–216. https://doi.org/10.2514/2.973.

[4] Fasel, H. F., Rist, U., and Konzelmann, U., "Numerical investigation of the three-dimensional development in boundary-layer transition," *AIAA Journal*, Vol. 28, No. 1, 1990, pp. 29–37. https://doi.org/10.2514/3.10349.

[5] Rist, U., and Fasel, H., "Direct numerical simulation of controlled transition in a flat-plate boundary layer," *Journal of Fluid Mechanics*, Vol. 298, 1995, p. 211–248. https://doi.org/10.1017/S0022112095003284.

[6] MA, Y., and ZHONG, X., "Receptivity of a supersonic boundary layer over a flat plate. Part 1. Wave structures and interactions," *Journal of Fluid Mechanics*, Vol. 488, 2003, p. 31–78. https://doi.org/10.1017/S0022112003004786.

[7] Bertolotti, F. P., Herbert, T., and Spalart, P. R., "Linear and nonlinear stability of the Blasius boundary layer," *Journal of Fluid Mechanics*, Vol. 242, 1992, p. 441–474. https://doi.org/10.1017/S0022112092002453.

[8] Day, M. J., "Structure and stability of compressible reacting mixing layers," Ph.D. thesis, Stanford University, California, Nov. 1999.

[9] Towne, A., Rigas, G., and Colonius, T., "A critical assessment of the parabolized stability equations," *Theoretical and Computational Fluid Dynamics*, Vol. 33, 2019. https://doi.org/10.1007/s00162-019-00498-8.

[10] Rigas, G., Colonius, T., and Beyar, M., "Stability of wall-bounded fows using one-way spatial integration of Navier-Stokes equations," *55th AIAA Aerospace Sciences Meeting*, 2017. https://doi.org/10.2514/6.2017-1881.

[11] Kamal, O., Rigas, G., Lakebrink, M. T., and Colonius, T., "Application of the One-Way Navier-Stokes (OWNS) Equations to Hypersonic Boundary Layers," *AIAA AVIATION 2020 FORUM*, 2020. https://doi.org/10.2514/6.2020-2986.

[12] Kamal, O., Rigas, G., Lakebrink, M., and Colonius, T., "Input/Output Analysis of Hypersonic Boundary Layers using the One-Way Navier-Stokes (OWNS) Equations," *AIAA AVIATION 2021 FORUM*, 2021. https://doi.org/10.2514/6.2021-2827.

[13] Kamal, O., Rigas, G., Lakebrink, M. T., and Colonius, T., "Input/output analysis of a Mach-6 cooled-wall hypersonic boundary layer using the One-Way Navier-Stokes (OWNS) Equations," *AIAA AVIATION 2022 Forum*, 2022. https://doi.org/10.2514/6.2022-3556.

[14] Sleeman, M. K., Lakebrink, M. T., and Colonius, T., "Nonlinear stability of wall-bounded flows using the One-Way Navier-Stokes (OWNS) Equations," *AIAA AVIATION 2023 Forum*, 2023. https://doi.org/10.2514/6.2023-3273.

[15] Towne, A., Rigas, G., Kamal, O., Pickering, E., and Colonius, T., "Efficient global resolvent analysis via the one-way Navier–Stokes equations," *Journal of Fluid Mechanics*, Vol. 948, 2022, p. A9. https://doi.org/10.1017/jfm.2022.647.

[16] Chang, C.-L., Malik, M. R., Erlebacher, G., and Hussaini, M. Y., "Linear and nonlinear PSE for compressible boundary layers," NASA Contractor Report 191537. Institute for Computer Applications in Science and Engineering (ICASE), September 1993.

[17] Joslin, R. D., Streett, C. L., and Chang, C. L., "Spatial direct numerical simulation of boundary-layer transition mechanisms: Validation of PSE theory," *Theoretical and Computational Fluid Dynamics*, Vol. 4, No. 6, 1993, pp. 271–288. https://doi.org/10.1007/BF00418777.

[18] Thompson, K. W., "Time dependent boundary conditions for hyperbolic systems," *Journal of Computational Physics*, Vol. 68, No. 1, 1987, pp. 1–24. https://doi.org/https://doi.org/10.1016/0021-9991(87)90041-6, URL https://www.sciencedirect.com/science/article/pii/0021999187900416.

[19] BERLIN, S., WIEGEL, M., and HENNINGSON, D. S., "Numerical and experimental investigations of oblique boundary layer transition," *Journal of Fluid Mechanics*, Vol. 393, 1999, p. 23–57. https://doi.org/10.1017/S002211209900511X.

[20] Chang, C.-L., and Malik, M. R., "Oblique-mode breakdown and secondary instability in supersonic boundary layers," *Journal of Fluid Mechanics*, Vol. 273, 1994, p. 323–360. https://doi.org/10.1017/S0022112094001965.

[21] Herbert, T., "Secondary Instability of Boundary Layers," *Annual Review of Fluid Mechanics*, Vol. 20, No. 1, 1988, pp. 487–526. https://doi.org/10.1146/annurev.fl.20.010188.002415.

[22] Sayadi, T., Hamman, C. W., and Moin, P., "Direct numerical simulation of complete H-type and K-type transitions with implications for the dynamics of turbulent boundary layers," *Journal of Fluid Mechanics*, Vol. 724, 2013, p. 480–509. https://doi.org/10.1017/jfm.2013.142.

[23] Huai, X., Joslin, R. D., and Piomelli, U., "Large-Eddy Simulation of Transition to Turbulence in Boundary Layers," *Theoretical and Computational Fluid Dynamics*, Vol. 9, 1997, pp. 149–163.

[24] Rigas, G., Sipp, D., and Colonius, T., "Nonlinear input/output analysis: application to boundary layer transition," *Journal of Fluid Mechanics*, Vol. 911, 2021, p. A15. https://doi.org/10.1017/jfm.2020.982.

[25] Klebanoff, P. S., Tidstrom, K. D., and Sargent, L. M., "The three-dimensional nature of boundary-layer instability," *Journal of Fluid Mechanics*, Vol. 12, No. 1, 1962, p. 1–34. https://doi.org/10.1017/S0022112062000014.

[26] Kachanov, Y. S., and Levchenko, V. Y., "The resonant interaction of disturbances at laminar-turbulent transition in a boundary layer," *Journal of Fluid Mechanics*, Vol. 138, 1984, p. 209–247. https://doi.org/10.1017/S0022112084000100.

[27] Bertolotti, F. P., "Linear and nonlinear stability of boundary layers with streamwise varying properties," Ph.D. thesis, The Ohio State University, Jan. 1991.

[28] Towne, A., and Colonius, T., "One-way spatial integration of hyperbolic equations," *Journal of Computational Physics*, Vol. 300, 2015, pp. 844–861. https://doi.org/https://doi.org/10.1016/j.jcp.2015.08.015.

[29] Briggs, R. J., "Electron-stream interaction with plasmas," , 1964.

[30] Kreiss, H.-O., "Initial boundary value problems for hyperbolic systems," *Communications on Pure and Applied Mathematics*, Vol. 23, No. 3, 1970, pp. 277–298. https://doi.org/https://doi.org/10.1002/cpa.3160230304.

[31] Zhu, M., and Towne, A., "Recursive one-way Navier-Stokes equations with PSE-like cost," *Journal of Computational Physics*, Vol. 473, 2023, p. 111744. https://doi.org/https://doi.org/10.1016/j.jcp.2022.111744, URL https://www.sciencedirect.com/science/article/pii/S0021999122008075.